photonics

MDPI

Article

Analysis of a Scanned, Single Beam, Spaceborne Topographic Lidar Providing Equally High Alongtrack and Crosstrack Resolution

John J. Degnan

Independent Researcher, Odenton, MD 21113, USA; jjdegnan3rd@gmail.com

Abstract

Virtually all spaceborne topographic lidars to date have used a single beam, with the exception of the ATLAS lidar on NASA's ICESat-2 satellite, which split the beam into 3 "strong" and 3 "weak" beamlets distributed perpendicular to the along-track path of the satellite. This approach has provided high-resolution along-track surface measurements but relatively poor resolution cross-track measurementswithin a given surface area. The present paper attempts to resolve this discrepancy by (1) transmitting and scanning a single Gaussian beam and (2) imaging the return onto a 14 × 14 pixelated, single-photon sensitive, detector array, thereby providing between 100 and 196 measurements per pulse, depending on the solar background. Besides enhancing the lidar's capability to penetrate tree canopies and water bodies, the proposed single-beam approach provides one to two orders of magnitude more measurements per pulse with equal spatial resolution in boththe along-track and cross-track directions. At the 10 kHz pulse rate of the ATLAS laser on NASA's ICESat-2 satellite, this implies between 1 and 2 million topographic measurements per second. The maximum surface area observable by a single pulse increases with the laser peak power defined by the ratio of the pulse energy to the temporal pulsewidth. Larger surface areas per pulse result in more time for cross-track scanning while still maintaining contiguous along-track mapping. Two scanning methods appear to be feasible: (1) circular scans using individual but temporally coordinated wedge scanners for the transmitted and received beams, and (2) unidirectional linear scans utilizing Acousto-Optic Deflectors. The circular scan approach is probably easier to implement, but it also requires additional post-processing to obtain an accurate contiguous 3D image of the planetary terrain.

Keywords: scanning spaceborne topographic lidar; single beam imaged onto pixelated detector; high spatial resolution; over 100 measurements per pulse

Check for updates

Received: 1 June 2026
Revised: 22 June 2026
Accepted: 23 June 2026
Published: 29 June 2026

Copyright: © 2026 by the author. Licensee MDPI, Basel, Switzerland. This article is an open access article distributed under the terms and conditions of the Creative Commons Attribution (CC BY) license.

1. Introduction

Very early in the 20th century, the first airborne, single-photon-sensitive lidar (Micro-Laser Altimeter or MLA) was developed at NASA Goddard Space Flight Center, using millimeteraccura satellite laserranging technologies developed over the prior 4 decades. The MLA used a single-wedge optical scanner and an early pixelated detector, i.e., a segmented-anode MicroChannel Plate PhotoMultiplier Tube (MCP/PMT), to record multiple, spatially resolved returns from a single laser pulse [1,2]. The potential for applying the technique to future space missions was immediately obvious, and a conceptual spaceborne lidar design utilizing a bidirectional linear scan created by two rotating optical wedges to direct both the transmitted and received beams was analyzed [3]. It was determined

however that, while a dual wedge scanning technique could effectively compensate for the roundtrip pulse time of flight and keep the returns centered on a single 10 × 10 detector array with a corresponding increase in the cross-track spatial coverage, there was an undesirable varying degree of overlap of the returns from consecutive pulses, with the maximum overlap occurring at the two ends of the linear scan due to the bidirectional nature of the linear scan. Shortly thereafter, the Jigsaw Program at MIT Lincoln Labs reported on a short-range (150 m) ground-based lidar which used a dual-wedge scanner [4] to keep the returning photons centered on a 32 × 32 pixel Geiger Mode Avalanche PhotoDiode (GMAPD) array.

In the ensuing decade, Sigma Space Corporation developed a series of successively higher-altitude airborne lidars operating at altitudes of roughly 1 to 7 km [5]. The earliest of these was named "Leafcutter", in which a 10 × 10 square array of 100 beamlets was generated by passing the 140 mW COTS (Commercial Off The Shelf) laser transmitter beam through an 80% efficient Diffractive Optical Element (DOE). Each beamlet contained approximately 1 mW of laser power, consisting of a 22 kHz stream of 700 ps FWHM, 50 nJ pulses. The ground images of the returning beamlets were optically matched to a COTS 10 × 10 segmentedanode MCP/PMT. The individual anode outputs were then input to an in-house multichannel timing receiver with an RMS timing/range precision of 23 ps/3.4 mm. Most importantly, the detector/receiver subsystem could record the arrival times of multiple, closely-spaced photons per channel with an event recovery time of only 1.6 ns. This made Leafcutter impervious to shutdown due to random solar events and also permitted multiple returns per channel from semi-porous volumetric scatterers, such as tree canopies. The solar noise per pixel was kept to a minimum through the use of a 0.3 nm FWHM spectral filter, a small receive telescope 7.5 cm in diameter, and a Field-of-View (FOV) per pixel limited by the nominal 15 cm × 15 cm ground pixel dimension which, over a nominal 1 km range, amounted to a solid angle of only 2.2×10^{-8} steradians per pixel. At the Leafcutter design AGL of 1 km, the interbeam spacing between beamlets at the surface was 15 cm, such that each laser pulse monitored a 1.5 m × 1.5 m surface area [5]. Later versions of Sigma's scanning airborne SPLs were designed to operate at altitudes up to 7 km, and the larger and more limited segmented anode MCP/PMT were replaced by newer Single Photon Avalanche Diode (SPAD) arrays. SPADs were chosen over Geiger Mode Avalanche PhotoDiodes (GMAPDs) based on analyses that suggested SPADs would provide superior tree-canopy penetration [5].

To the author's knowledge, all but one spaceborne topographic lidar to date have used a single short-pulse laser beam whose return from the underlying surface was imaged onto a single multiphoton sensitive detector, thereby limiting the surface detection rate to the laser pulse rate, which was typically several tens of pulses per second. At typical spacecraft speeds, the resulting along-track resolution is modest at best, especially at low orbital altitudes where satellite velocities are highest. Furthermore, modest cross-track resolution can only be achieved after many orbital passes over the same terrain. However, NASA's ATLAS lidar on the ICESat-2 satellite, launched into a 500 km high orbit in September 2018 [6], used a single low-energy per pulse (500 μJ) frequency-doubled Nd:YVO laser operating at a 10 kHz rate. Each laser pulse was then split into 3 pairs of "weak/strong" beamlets. The green wavelength at 532 nm was stationed well within the "atmospheric window" for low attenuation of the lidar beam and also allowed bathymetric measurements in water bodies of modest depth. The weak beamlets each consisted of a 10 kHz train of 34 μJ pulses, while the 3 "strong" beamlets contained a 10 kHz train of 133 μJ pulses. Thus, the six beams were capable of generating an unprecedented 60,000 surface measurements per second, i.e., roughly 3 orders of magnitude greater than prior multiphoton spaceborne lidars.

Within each pair, the weak and strong beams are separated by about 90 m in the cross-track direction, while the cross-track distance between pairs is about 3 km. In contrast, the measurements in the along-track direction are separated by only 70 cm due to the high 10 kHz pulse repetition rate and the satellite velocity at the 500 km satellite altitude. Incredibly, the ATLAS laser has operated with little or no degradation in performance over the 7-plus years since the ICESat-2 launch in September 2018 and has accumulated roughly 3 trillion surface measurements to date. In a recent article [7], the present author discussed how the ATLAS lidar technology might be used to map other planets in our solar system while, for periods of several months, continuously transmitting data back to a satellite in a quasi-synchronized Earth orbital plane parallel to the planetary orbital plane. The same article also briefly introduced a potential alternative approach: using a single quasi-Gaussian lidar beam whose return is imaged onto a highly pixelated, single-photon-sensitive detector with the goal of achieving a much higher surface measurement rate, leading to equal and or higher spatial resolution in both the along-track and cross-track directions. In this article, the relevant technologies and equations for this alternative approach are derived and applied to a possible future Earth orbiting satellite demonstration, which could potentially lead to other high-resolution topographic maps of planets (or moons) throughout our solar system.

2. Worst Case Signal to Noise Ratio

As described in a previous publication [7], the worst-case *SNR* only occurs when the solar photons follow the same two-way path to the surface as the lidar beam, which is always pointed roughly toward the center of the Earth. As illustrated in Figure 1, this occurs only once per year in each of the Northern and Southern latitudes when the satellite intercepts the line joining the centers of the Earth and Sun. Since the rotational axis of the Earth is displaced by roughly 17° from the normal to the Earth's orbital plane about the Sun, the highest solar background occurs only twice per year as the satellite passes over Northern and Southern latitudes of +/−17 degrees and diminishes to zero via the factor $\cos\left\lfloor \text{lat} + / - 17^{\circ} \right\rfloor$. Between these latitudes, the lidar observes a gradual reduction in the solar background until the satellite enters the night hemispherewhere the solar background is zero. The number of received lidar photons per pulse has been shown to be equal to [7]

$$n_R = n_T(\eta_T\eta_R\eta_D)g_T g_R A_p^2 \frac{1}{(\lambda z)^2}[T_{atm}^2\rho_s(\lambda)\cos(\psi)] = 0.36\, n_T\left(\frac{A_P}{\lambda z}\right)^2[T_{atm}^2\rho_s(\lambda)\cos(\psi)] \quad (1)$$

where n_T is the number of photons transmitted per laser pulse; the product $\eta_T\eta_R\eta_D$ = 0.65 × 0.65 × 0.7 = 0.30 represents the typical optical efficiencies of the lidar transmit and receive optics and the single-photon-sensitive detector respectively; g_T = 1.12 and g_R = 1 are the optimum Gaussian beam transmit/receive efficiencies of a common lidar telescope with no secondary mirror, Ap is the area of the common transmit/receive telescope (if appropriate) primary lens/mirror; λ is the lidar wavelength; z is the lidar orbital altitude, $T_{atm}^2(\lambda)$ is the two-way atmospheric transmission of the planetary atmosphere; ρ_s is the reflectance of the planetary surface illuminated by the laser; and ψ is the surface slope. Meanwhile, the number of solar photons collected during the duration of the laser pulse τ_p is given by

$$n_s = S_E\Delta\lambda\tau_p\frac{\lambda}{hc}A_P[T_{atm}^2\rho_s(\lambda)\cos(\psi)] \quad (2)$$

where $S_E(\lambda)$ is the solar irradiance as it enters the Earth's atmosphere, measured in Watts/(m^2 nm), $e_p = hc/\lambda$ is the photon energy at the laser wavelength λ, τ_p is the laser pulsewidth, and $\Delta\lambda$ is the lidar receiver spectral filter bandwidth. Dividing Equation (1) by Equation (2) gives an equation for the worst-case SNR, i.e.,

$$SNR_{wc} = \frac{0.36\, n_T}{S_E(\lambda)\Delta\lambda\tau_p}\frac{hc}{\lambda}\frac{A_P}{(\lambda z)^2} \quad (3)$$

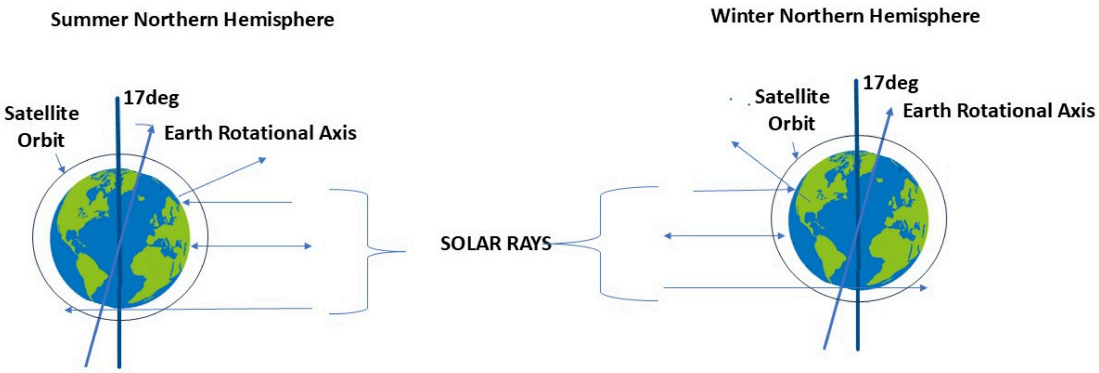

Figure 1. The worst-case SNR occurs when the lidar photons and solar photons travel a common round-trip path to the surface and therefore experience roughly the same atmospheric and surface reflectivity/slope losses. This occurs twice per year when the Earth, Sun, and satellite all lie on a common line, i.e., when the angle θ = 0 or π and the satellite latitude satisfies the condition cos(lat −17°) = 1 in the Northern Hemisphere and cos(lat +17°) in the Southern Hemisphere.

Figure 2 illustrates how the worst-case signal-to-noise ratio per orbit improves by a factor of $1/\cos\theta$ as the Earth (or any other planet) orbits the Sun. As θ approaches 90 or 270 degrees, the solar photon count from solar scatter off the surface is greatly reduced by a factor of $1/\cos\theta$ since the solar photons travel roughly parallel to the planetary surface and can only enter the lidar receiver via scattering off molecules in the intervening atmosphere. Furthermore, whereas the ATLAS lidar was able to determine the along-track surface within a background of random solar photons, the approach proposed here should permit the proper identification of a three-dimensional surface, i.e., in both the along-track and cross-track dimensions, within a single laser pulse, and further tying them to spatially adjacent pulses.

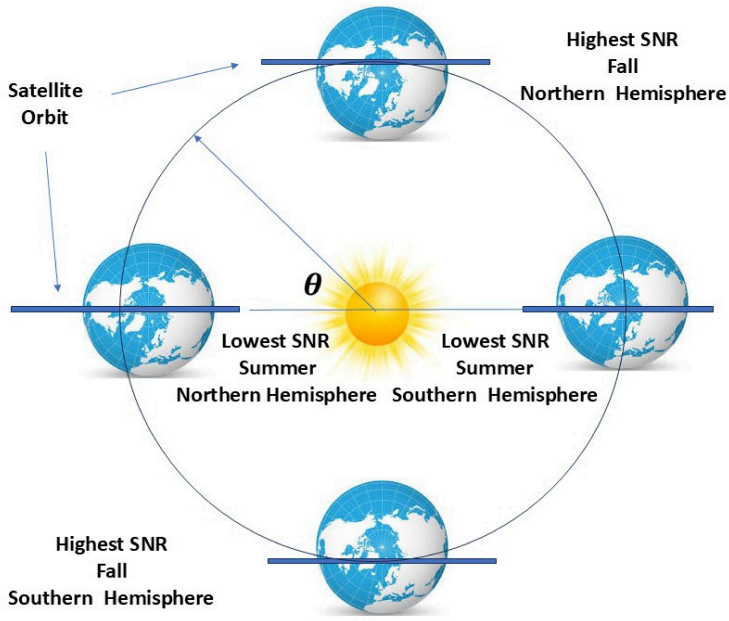

Figure 2. As the Earth orbits the Sun, the angle θ between the Sun and satellite orbital plane changes, causing the worst-case solar background per orbit to be reduced by a factor $|cos\theta|$. The worst-case SNR occurs twice per Earth orbit when the satellite intercepts the Earth's orbital plane about the Sun on the side closest to the Sun, i.e., when θ = 0° and 180°.

Obviously, another important consideration is the choice of laser wavelength. The latter depends on several factors including: (1) high transmission through the atmosphere; (2) the spectral distribution and relative intensity of competing solar radiation impinging on the atmosphere; (3) whether or not shallow water bathymetry and therefore high transmission in lake, river, bay or ocean waters is a mission requirement; and (4) the availability of a suitable high peak power, ultrashort pulse laser in the nanosecond to picosecond regime at the desired wavelength. Fortunately, various sources have provided an extremely helpful plot reproduced in Figure 3 [8]. In that figure, the yellow profile shows the intensity of solar irradiance $S_E(\lambda)$ versus wavelength as it enters the atmosphere, while the corresponding black curve represents the black body temperature of 5780 K that best approximates the solar spectral output. The solar irradiance, $S_E(\lambda)$, peaks at about 2W-m^2 nm^{-1} at a wavelength slightly less than 500 nm. However, even without additional attenuation by intervening clouds, fog, or dust, only 65% reaches the surface due to atmospheric absorption and/or scattering. On the other hand, the solar irradiance drops rapidly as one moves away from visible wavelengths toward the ultraviolet or infrared. The red profile in Figure 3 describes the solar spectral distribution at sea level, and we note two potential advantages of near-infrared wavelengths near 1000 nm, 1200 nm, 1500 nm to 1700 nm, and 2100 nm. In these wavelength bands, not only is the solar background significantly reduced relative to the visible wavelengths, but the one-way atmospheric transmission is closer to 100% than at visible wavelengths. On the other hand, none of these longer wavelengths are suitable for bathymetry if that is a mission priority. In any event, depth penetration will likely be limited to a few tens of meters, even in clear waters, when optimal green wavelengths are used.

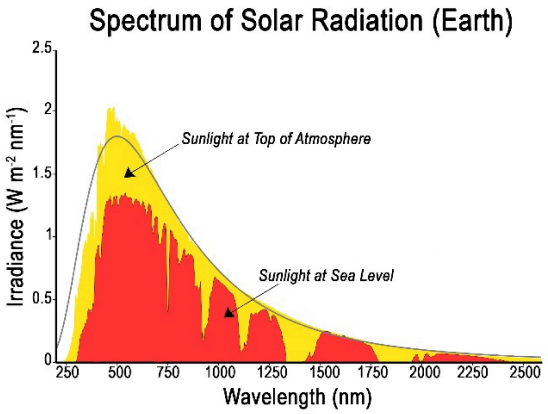

Figure 3. Graph showing the solar irradiance as it enters the Earth's atmosphere in yellow, the solar irradiance at sea level in red, and a black line indicating the irradiance of a black body at a temperature of 5780 degrees Kelvin. Wavelengths where the red is close to touching the black line are of interest because (1) the solar irradiance is quite low and (2) there is very little absorption or scattering by the atmosphere, suggesting that very high Signal toNoise Ratios (SNRs) are possible over land masses or water surfaces at infrared wavelengths.

3. Single Beam Lidar Imaged onto a Single Photon Sensitive Array

We now consider the feasibility of a lidar projects a reasonably large Gaussian beam onto the surface but views the return image with a single photon sensitive detector array with the goal of making a high spatial resolution 3D image in both the along-track and cross-track directions with each laser pulse. As the SNR increases dramatically within a given satellite orbit or as the Earth orbits the Sun, presumably more surface measurements can be made per pulse for (1) a fixed beam diameter on the planetary surface or, if necessary, (2) a variable diameter based on the Earth's orbital position about the Sun. We will now study the first and simpler option in detail.

The radius w_s of a transmitted Gaussian TEM$_{00}$ laser beam with wavelength λ and an initial waist radius w_0 to the $1/e^2$ intensity points grow in size as the beam travels from a satellite at altitude z to the planetary surface according to the equation [9].

$$w_s = w_0\sqrt{1+\left(\frac{\lambda z}{\pi w_0^2}\right)^2} \cong \frac{\lambda z}{\pi w_0} \tag{4}$$

where w_0 is the radius to the $1/e^2$ intensity point of the Gaussian laser beam leaving the spaceborne lidar, λ is the laser wavelength, z is the orbital altitude of the host spacecraft, and the approximation is valid for large values of z. The derivative of Equation (4) with respect to z, i.e., $\lambda/\pi w_0$, can be interpreted as an extremely small angle of incidence of lidar photons at the lidar beam's waist w_s ($1/e^2$ intensity point) striking the planetary surface.

In the worst-case SNR scenario, solar photons follow paths parallel to those of the laser photons and therefore experience the same round-trip surface and atmospheric/sea penetration losses given by the equation.

$$Loss \cong \left[T_{atm}^2\ \rho_w\ T_{water}^2\ \rho_s\ cos\beta\right] \tag{5}$$

where ρ_w and ρ_s are the reflectivities of the water (if any) and land surfaces, respectively, and β is the angle of the surface slope.

If we now include round-trip atmospheric transmission losses, a planetary surface having a reflectivity ρ_s and slope β, and a lidar receive aperture A_R, we obtain the following equation for the density of lidar photons collected by the receive telescope (Lidar Signal) with area A_R.

$$LS(r_s) = \frac{E_T}{\tau_p}\left(\frac{2}{\pi w_s^2}exp\left(-2\frac{r_s^2}{w_s^2}\right)\right)[A_R Loss] = \frac{E_T}{\tau_p}\alpha\ exp\left[-\alpha r_s^2\right]A_R Loss \tag{6a}$$

where τ_p is the laser pulsewidthand we have defined the variable

$$\alpha\ \frac{2}{\pi w_s^2} \equiv \frac{2}{A_s} = \frac{2}{\pi}\frac{(\pi w_0)^2}{(\lambda z)^2} = \frac{2A_T}{(\lambda z)^2} \tag{6b}$$

where, from Equation (4), A_s is the Gaussian beam area at the planetary surface and the laser pulse energy E_T is contained within an ultrashort Q-switched or mode-locked pulse with temporal width τ_P, typically measured in nanoseconds to picoseconds for maximum range accuracy, and $A_T = \pi w_0^2$ is the area of the transmitted Gaussian laser beam as determined by the $1/e^2$ intensity radius. We will now compute the value of α that maximizes the area of the beam on the planetary surface that always sees a worst-case SNR greater than or equal to 1.

The solar irradiance $S_E(\lambda)$, plotted in Figure 3, is expressed in units of Watts/(m^{2}nm) = Joules/(sec-m^2-nm). The solar background is reduced through the use of a bandpass filter having a narrow width of $\Delta\lambda$. typically expressed in nm. Since the atmospheric and water transmissions and reflections off water or solid surfaces are experienced equally by the lidar and solar αphotons under worst-case solar conditions, they do not affect the SNR. Furthermore, the aperture of the receive telescope amplifies the number of lidar and solar photons equally without affecting the SNR. Dividing Equation (6a) by Equation (6b) yields the worst-case SNR as a function of the radius r_s within the ground area illuminated by the Gaussian laser beam, i.e.,

$$SNR_{wc}(r_S) = \frac{LS(r_S)}{S_E(\lambda)(\Delta\lambda)[A_R Loss]} = \frac{E_T}{\tau_p}\frac{\left[\alpha\ exp\left(-2\alpha r_s^2\right)\right]}{S_E(\lambda)(\Delta\lambda)} = C\alpha\ exp\left(-2\alpha r_S^2\right) \tag{7a}$$

where we have introduced the constant

$$C = \frac{E_T}{\tau_p}\frac{1}{S_E(\lambda)(\Delta\lambda)} \tag{7b}$$

which has units of $m^{2,}$ and the product $C\alpha$ is unitless. We now wish to find the value of r_S that maximizes the surface area, providing an $SNR_{wc} \geq 1$. Setting Equation (7a) equal to 1 and taking the natural log of both sides of the resulting equation yields

$$ln(C\alpha) - 2\alpha r_s^2 = 0 \tag{8}$$

Solving Equation (8) for r_s^2, we obtain the worst-case surface area having an SNR ≥ 1, i.e.,

$$A_{wc} = \pi r_s^2 = \frac{\pi}{2\alpha} \ln(C\alpha) = \frac{\pi C}{2} \frac{ln(x)}{x} \tag{9a}$$

where we have defined the dimensionless variable x = Cα. Taking the derivative of Equation (9a) with respect to x and setting the result equal to zero yields x = e = 2.71828. Thus, the maximum achievable worst-case surface area with SNR > 1 is equal to

$$A_{max} = \frac{\pi C}{2} \frac{ln(x)}{x} = \frac{\pi C}{2e} = 0.577\ C \tag{9b}$$

when

$$x \equiv C\alpha = \frac{CA_T}{(\lambda z)^2} \equiv \frac{2C}{A_{max}} = \frac{2}{0.577} = 3.47 \tag{9c}$$

where A_{max} is the maximum achievable area of the Gaussian beam at the planetary surface via Equation (6b), C and A_T are in units of m^2, and the area A_{max} is obtained by differentiating Equation (9a) with respect to α and setting the result equal to 0. As one would expect, A_{max} shrinks to zero if $C = 0$. It is also important to note from Equation (7a) that the value of C is proportional to the peak power of the laser E_T/τ_p and not the pulse energy alone. Thus, a significantly shorter pulse, such as a picosecond pulse from a modelocked laser, would require 1000 times less energy than a nanosecond pulse from a Q-switched laser to achieve the same SNR.

4. Minimum Size of the Detector Array and Number of Pixels

We now return to the worst-case SNR scenario and assume that a square single photon sensitive detector array consisting of $n_a \times n_a$ pixels is placed in the image plane of the lidar receive telescope, as in Figure 4, such that the four corners of the square array coincide with the circle corresponding to the radius r_{wc}, where the SNR_{wc} equals 1. Although the spatial resolution of the measurements clearly increases with the number of pixels contained within the image of the lidar return, too small a pixel may result in too few lidar photons to allow a confident range measurement. Clearly, the weakest SNR occurs at the corners of the square array and is approximately equal to the SNR at the center of the corner pixel multiplied by the area of the pixel δ^2. Using Equation (7a).

$$SNR_{min} = \left[SNR_{wc}\left(r_s - \frac{\delta}{\sqrt{2}}\right)\right] = C\alpha\ exp\left[-2\alpha\left(r_s - \frac{\delta}{\sqrt{2}}\right)^2\right] = C\alpha\ exp\left[-(n_a - 1)^2\alpha\delta^2\right] \tag{10a}$$

Taking the natural logarithm of both sides yields

$$(n_a - 1)^2\delta^2 \equiv (d_s - \delta_s)^2 = \frac{1}{\alpha} ln\left(\frac{C\alpha}{SNR_{min}}\right) = \frac{A_{wc}}{2} ln\left(\frac{2C}{A_{max} SNR_{min}}\right) \leq \frac{A_{max}}{2} ln\left(\frac{2C}{A_{max}}\right) \tag{10b}$$

under worst-case solar background conditions, where the subscript s implies the projection of the array onto the planetary surface. Taking the square root of both sides of Equation (10b), we can solve for the corner pixel size projected onto the planetary surface, $\delta_{s,}$ that meets the desired minimum SNR requirement, i.e.,

$$\delta_s = d_s - \sqrt{\frac{A_{wc}}{2} ln\left(\frac{2C}{A_{wc} SNR_{min}}\right)} = d_s - \sqrt{\frac{A_{wc}}{2}\left[ln\left(\frac{2C}{A_{wc}}\right) - ln(SNR_{min})\right]} \geq d_s - \sqrt{\frac{A_{wc}}{2}\left[ln\left(\frac{2C}{A_{wc}}\right)\right]} \tag{11}$$

or alternatively, the number of pixels per dimension, i.e., along-track or cross-track

$$n_{wc} \equiv \frac{d_s}{\delta_s} = \frac{d_s}{d_s - \sqrt{\frac{A_{wc}}{2}\left[ln\left(\frac{2C}{A_{wc}} - ln(SNR_{min})\right)\right]}} = \frac{1}{1 - \sqrt{\frac{A_{wc}}{2d_s^2}\left[ln\left(\frac{2C}{A_{wc}}\right) - ln(SNR_{min})\right]}} \leq \frac{1}{1 - \sqrt{\frac{\pi}{4}\left[ln\left(\frac{2C}{A_{wc}}\right)\right]}} \quad (12a)$$

Equations (11) and (9b) indicate that the largest number of pixels is obtained when $A_{wc} = A_{max} = 0.577C$, resulting in

$$n_{wc} = \frac{1}{1 - \sqrt{\frac{\pi}{4}\left[ln\left(\frac{2C}{A_{max}}\right)\right]}} = \frac{1}{1 - \sqrt{\frac{\pi}{4}\left[ln\left(\frac{2C}{0.577C}\right)\right]}} = \frac{1}{1 - \sqrt{\frac{\pi}{4}[ln(3.46)]}} = \frac{1}{1 - \sqrt{0.973}} = 10.6 \quad (12b)$$

Thus, choosing the maximum area allowed under worst-case solar background conditions, A_{max} results in a 10 × 10 array of pixels, all having an SNR > 1. This is a factor of 100/6 = 16 times more measurements per pulse than was achieved by splitting the ATLAS lidar pulse into 3 "strong" and 3 "weak" beams. Furthermore, as will be demonstrated in the next section, this advantage will only increase as the satellite moves away from its worst-case position.

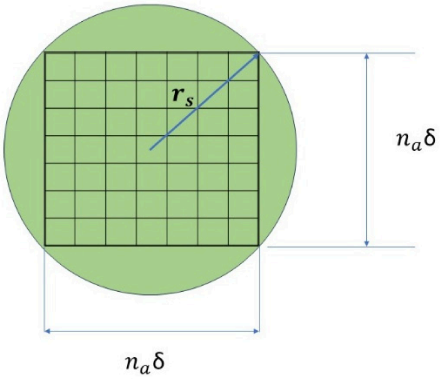

Figure 4. Instead of splitting the lidar beam into separate beamlets, one can choose to image a single-beam lidar return onto a square, single photon sensitive detector array [2]. We will demonstrate that, compared to the 6-beam approach used in NASA's ICESat 2 mission, the detector array can provide 1 to 2 orders of magnitude more surface measurements per pulse with uniform spatial resolution in both the along-track and cross-track dimensions over large surface areas.

5. Expanding the Worst Case Detector Array Size to Take Advantage of Decreased Solar Backgrounds

The calculations presented so far have assumed a worst case solar noise situation which, as described in Figures 1 and 2, only briefly occurs twice per year when the satellite position intercepts the line connecting the centers of the Sun and the planet under investigation, As discussed in Section 2 of this paper; however, the lidar sees a solar background decreasing by the factor cosφ as the satellite progresses in its own orbit about the planet and by an additional factor of cosθ as the planet orbits the Sun. As discussed previously, this is due to the fact that the reflected solar photons no longer follow a path parallel to that of the lidar photons, which are always directed roughly toward the planet's center of mass and therefore roughly orthogonal to the surface. This effect can be accounted for by replacing the constant C by C secφ secθ in all previous equations, but keeping the same value of $\alpha \equiv A_T/(\lambda z)^2 \equiv 2/A_{max}$ since the transmitted beam area A_T, the wavelength λ, and satellite altitude z all remain constant. The surface area per pulse having an SNR greater than 1 is now given by the equation

$$A_{wc}(\varphi, \theta) = \frac{\pi}{2\alpha}\ln(C\alpha\, sec\varphi\, sec\theta) = \frac{\pi}{2\alpha}\ln(C\alpha)\left[1 + \frac{ln(sec\varphi\, sec\theta)}{\ln(C\alpha)}\right] = A_{max}\left[1 + \frac{ln(sec\varphi\, sec\theta)}{\ln(C\alpha)}\right] \quad (13)$$

In the previous section, we derived the maximum surface coverage per pulse (A_{max}) under the worst-case solar background (φ = θ = 0°). Using the same value of $C\alpha$ in Equation (13), we see that the areal coverage per pulse will be doubled if

$$sec\varphi\, sec\theta = C\alpha \equiv CA_T/(\lambda z)^2 \equiv \frac{2C}{A_{max}} \quad (14)$$

The typically huge value of C indicates that increasing the size of the detector array in both the along-track and cross-track directions by a factor of $\sqrt{2}$ will increase the number of pixels (and measurements per pulse) by almost an additional factor of 2, i.e., 196 measurements per pulse, as the solar background decreases during the worst-case satellite orbit (θ = 0) and even more frequently as the Earth orbits the Sun (θ not equal to 0 or 180 degrees). Furthermore, as the Earth orbits the Sun ($0 \leq \theta \leq 360$ degrees) and rotates about its axis, surfaces initially subjected to worst-case solar irradiance will be periodically revisited with decreased solar background during subsequent Earth orbits.

6. Example: Impact of the ATLAS Laser Characteristics on Areal Coverage

As mentioned in the Introduction, the ATLAS lidar on NASA's ICESat -2 satellite has demonstrated remarkable longevity, operating at a pulse rate of 10 kHz for over 6 years of operation with little or no degradation since its launch in September 2018. The ATLAS laser on ICESat-2 is a frequency-doubled, Q-switched, Nd:YVO_4 laser operating at a green wavelength (λ = 532 nm) and producing 5W of power, consisting of a 10 kHz train of 1.5 nsec pulses, each containing 500 microjoules of energy. Thus, the number of photons per 500 microjoule pulse is $n_T = 1.34 \times 10^{15}$. From the following equations, we compute several key parameters

Equation (7b) $$C = \frac{5\times10^{-4}\ J}{1.5\times10^{-9}\ sec}\ \frac{m^2 sec}{1.8\ J}\ \frac{nm}{1.5\ nm} = 1.23 \times 10^5\ \mathrm{m}^2$$

Equation (9b) $$A_{max} \equiv \tfrac{\pi}{4} D_{max}^2 = 0.577\ C = 7108\ \mathrm{m}^2 = \text{maximum surface area having SNR}_{wc} > 1$$

$$d_{max} \equiv n_a \delta = \frac{D_{max}}{\sqrt{2}} = 67.2\ \mathrm{m} = \text{maximum worst-case dimension of the array projected onto the surface}$$

$$d_{exp} = \sqrt{2} d_{max} = 95\ \mathrm{m} = \text{expanded array dimension to accommodate decreased solar background}$$

Equation (9c) $$\alpha_{max} \equiv \frac{A_T}{(\lambda z)^2} \equiv \frac{2}{A_{max}} = \frac{3.47}{C} = 2.82 \times 10^{-5} \mathrm{m}^{-2}$$

Assuming the ATLAS lidar wavelength of λ = 532 nm and altitude z = 500 km in Equation (9c), we obtain a transmitted beam area of A_T = 2 mm^2 corresponding to a Gaussian beam diameter of only 1.6 mm, further demonstrating the beneficial impact of a high peak power laser on the value of the constant C.

7. Applying the Dual Wedge Scanner to Spaceborne Altimeters

The velocity of a satellite orbiting the Earth is given by the equation

$$v_s\ (z) = \sqrt{\frac{GM_p}{(r_p + z)}} = \sqrt{\frac{GM_p}{r_p}} \frac{1}{\sqrt{1 + \frac{z}{r_p}}} = \frac{7.91\ \mathrm{km}}{\mathrm{sec}} \frac{1}{\sqrt{1 + \frac{z}{r_p}}} \tag{15}$$

where the Gravitational Constant $G = 6.6743 \times 10^{-20}$ km^3 /kg sec^2, $M_P = 5.972 \times 10^{24}$ kg is the Earth's planetary mass, r_p = 6371 km is the Earth's radius, and z is the satellite altitude above the surface. For values of z much less than the planetary radius where spaceborne lidars are most effective, the satellite velocities vary only by a few percent since the ratio of satellite altitude to planetary radius is usually quite small. For example, the ICESat-2 satellite at an altitude z = 500 km travels at a velocity of roughly 7.62 km/s, only 3.7 percent less than the unachievable maximum value of 7.91 km/s at z = 0 km. Ignoring the slightly slower velocity of light within our relatively thin atmosphere and variations in the surface elevation, the roundtrip propagation time of the laser pulse between the satellite and the surface is roughly τ = 3.33 msec, during which time the ICESat-2 satellite travels a distance of 25.4 m, corresponding to an angular displacement between the transmitted and received beams of tan(β) = 25.4 m /500 km = 5.08×10^{-4} or β = 0.0291 deg. Therefore, during the 10^{-4} s interval between pulses, the ICESat-2 satellite traveled only 0.762 m. However, the maximum dimension of the array, d_{exp} = 95 m for a single pulse, derived in the previous section, is a factor of 124 larger than the along-track displacement between pulses, indicating that there would be roughly 124 overlapping pulses in the along-track direction, providing repetitive, rather than additional, information on the underlying terrain. On the positive side, however, any significant overlap in the along-track direction suggests that the spatial extent of the cross-track measurements could be greatly expanded by scanning the beam. Furthermore, splitting the beam into a large number of beamlets by a diffractive element and using a dual wedge scanner to compensate for point ahead due to the finite

speed of light, as in previously describedrborne instruments [5], would be impractical since the small diameter of the transmitted beams would, according to Equation (4), be spread over a much wider surface area thereby greatly reducing the overall SNR per pixel. On the other hand, scanning a single and larger diametertransmitter beam via a dualwedge scanner and imaging the returning photons from each pulse onto a single square, 14 × 14 pixel detector array would preserve the high SNR and spatial resolution discussed in previous sections.

Maximum spatial coverage is obtained by illuminating a surface area equal to A_{max}, defined by Equation (9b) and completing a circular dual wedge scan in a time interval equal to 124×10^{-4} s = 0.0124 s, corresponding to a modest scanner rotational speed of 80.6 rpm. During that time interval, the ICESat-2 satellite travels a distance of 95 m, equal to the expanded array dimension d_{exp} projected onto the planetary surface, thereby confirming contiguous along-track mapping. Thus, the cross-track mapping can be extended a maximum distance of ±5.9 km (11.8 km total) from the along-track path with the same spatial resolution. If desired, spatial resolution can be traded off against spatial coverage by simultaneously (1) increasing the diameter of the transmitted beam to create a smaller beam area on the surface (which also increases the SNR per pixel) and (2) reducing the diameter of the conical scan. It must also be mentioned that, because of the significantly higher spacecraft ground velocities relative to aircraft velocities, each successive array image in the circular scan is displaced in the positive along-track direction by an amount $v\Delta t$ = 7.62 m and must therefore be accounted for when generating the final contiguous 3D image of the underlying terrain. In the following section, we discuss unidirectional linear scanning methods that could potentially eliminate the need for such arduous corrections. While a dual-wedge scanner can generate a linear scan, it is bidirectional and cannot maintain the necessary look-ahead angle between the transmit and receive beams, and the use of wedge scanners must therefore be limited to unidirectional circular scans.

8. Unidirectional Linear Scan Options

Figure 5 illustrates a simplified situation where only 4 pulses are scanned in the cross-track direction (n_c = 4) before returning to the initial scan position. Each numbered square in the Figure corresponds to a single laser pulse imaged onto the nominal extended 14 × 14 pixel square array to obtain an accurate 3D image of the terrain illuminated by that pulse. However, if the cross-track linear scan is orthogonal to the ground track, the overall 3D image of the surface within a single scan is awkwardly segmented and must be combined with many other scans to form a complete image over an extended surface area. However, by tilting the cross-track scan slightly to the rear by an angle equal to $\tan(\psi) = 1/(n_c - 1)$, each image from a single scan can be easily combined to form a simple rectangular image of the total surface viewed by the scan. Each of the linear scans can then be easily combined to provide accurate 3D images of larger areas. Of course, in order for all of the pulse returns to be imaged onto a single 14 × 14 pixel array, the transmitter scan must be advanced relative to the receiver scan by a time interval equal to the roundtrip travel time of the pulse between the satellite and the surface (often referred to as "look ahead"). For the 500 km ICESat-2 orbit, the temporal "look ahead" would be 3.33 msec, whereas the total scan time interval would be equal to $n_c \times 10^{-4}$ s = 12.4 msec. The maximum scan angle ψ required during that period is given by the equation

$$tan\left(\frac{\psi}{2}\right) = \frac{(n_c - 1)}{2}\frac{d_{exp}}{z} = 0.0117 \quad (16)$$

which yields a value ψ = 1.30 deg = 22.7 mrad and an angular speed of 22.7 mrad/12.4 msec = 1.83 rad/s.

A review paper published in 2014 [10] provides a useful comparison of 9 different laser scanning techniques, only 2 of which can meet the desired beam aperture and deflection angle requirements while providing a truly unidirectional linear scan, i.e., one that does not require a reversal of the scan direction to initiate subsequent scans that would disrupt the continuity of the point ahead angle. The two candidates are (1) the rotating Polygon Mirror (PM) [11] and (2) the Acousto-Optic Deflector (AOD). As illustrated in Figure 6, each face of the PM scanner must be wide enough to contain the outgoing laser beam diameter, i.e., 2 to 10 mm depending on the satellite altitude and desired beam diameter on the planetary surface, and long enough to reflect n_c slightly overlapping pulses of the same diameter in a single scan. The short angular scans, generated by each face of the polygon and combined with the large number of beam diameters per face, would require a rotating polygon

measuring more than 6 m in diameter even at orbits as low as 250 km. The AOD, on the other hand, illustrated in Figure 7, is much more compact, can currently accept beam diameters up to 10 mm, and can generate rapid unidirectional linear scans. Table 1 lists the desired scan characteristics for a lidar in a 500 km orbit.

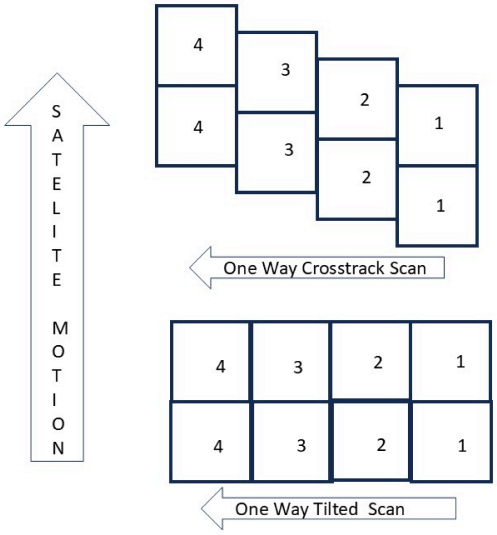

Figure 5. Because of the along-track motion of the host satellite, each successive cross-track pulse (indicated by the numbers 1 to 4) in the top figure is displaced in the forward direction by a distance d_{exp}/n_c, where d_{exp} is the dimension of the expanded, single pulse, 14 × 14 pixel square array projected onto the planetary surface and $n_c = 4$ is the assumed number of cross-track pulses. By tilting the angle of the right-to-left cross-track scan slightly to the rear, all of the surface measurements can be made by a simple rectangular array, as in the bottom figure, whose cross-track length is n_c times that of the along-track length d_{exp}. The tilt angle ε decreases as the number of pulses per crosstrack scan n_c increases according to the formula $\tan(\varepsilon) = \tan[1/[(n_c - 1)]]$.

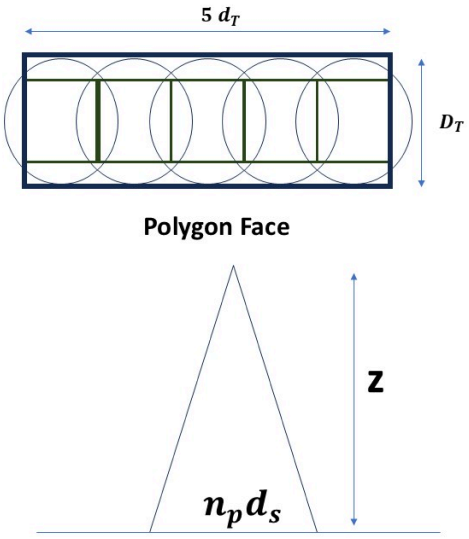

Figure 6. For the polygon mirror scanner, each face must accommodate the number of cross-track pulses ($n_p = n_c - 1$) used in the scan, where, for simplicity, $n_p = 5$ in the figure. Since the satellite altitude z is always far greater than the scanned length on the planetary surface, the scan angle is very small. Therefore, an unrealistically huge rotating polygon, measuring several meters in diameter with many faces, would be required to accommodate a large number of pulses per scan. In addition, the two Gaussian-shaped laser pulses on either end of a given face would have to be truncated, as in the top part of the figure, thereby distorting the shape of the ground distribution at both ends of the linear scan.

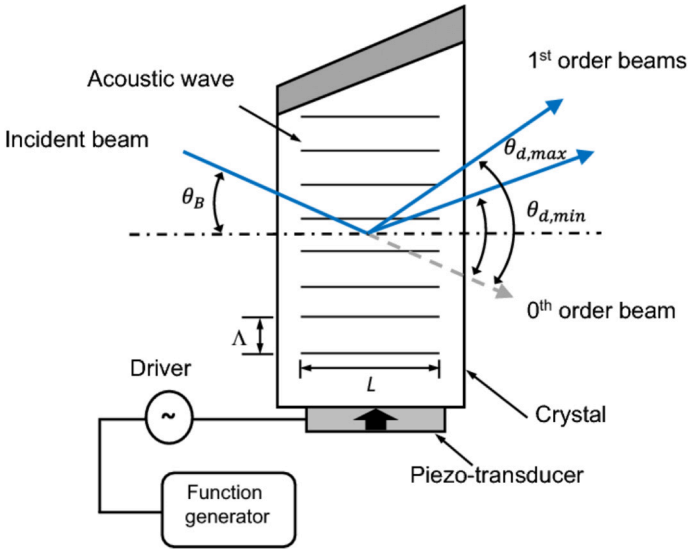

Figure 7. Schematic of an Acousto-Optic Deflector (AOD) system showing the laser deflection (From Ref. [7]).

Table 1. Cross-track Scanner Requirements for the ATLAS/ICESat-2 Operational Scenario at 500 km Altitude.

Transmit Beam Diameter	Maximum Scan Angle	Pulses per Scan	Scan Interval	Scan Speed
2 to 10 mm	1.30 deg 22.7 mrad	124	12.4 msec	105 deg/s 1.83 rad/s

In summary, comparing the requirements in Table 1 with the capabilities and limitations of the various scanning mechanisms provided in [11], the Acousto-Optical Deflector (AOD) appears to be best suited to the current application [11–13], i.e., the AOD has no moving mechanical parts and is capable of high angular deflection velocities and accuracies. Furthermore, it can (1) accommodate beam diameters up to 10 mm, (2) provide deflection angles up to 50 mrad (over 2 times greater than the 22.7 mrad needed for the maximum achievable cross-track coverage with the ATLAS laser) and (3) has the capability of resolving up to 500 individual pulses per scan as compared to the maximum achievable number n_c = 124 in the current application. In fact, the Model H-424 AOD, sold commercially by the US corporation L3 Harris [14], is suitable for use at the 532 nm ATLAS wavelength and can accommodate a 2 mm diameter beam vs. the 1.6 mm minimum requirement in Table 1 and an angular range of 33 mrad vs. the 22.7 mrad requirement. The latter device seems ideal for experimental airborne platforms and possibly for future satellite missions following space qualification.

9. Extension to Other Planets and Moons in Our Solar System

Extending the calculations presented here to other planets in our solar system is quite simple. As mentioned previously, different atmospheric transmissions and/or surface reflections cancel out of the equations for the *SNR* unless the planetary atmosphere or clouds totally block the laser wavelength. Only three parameters change with respect to the calculations presented here. The first is the distance of the planet from the Sun, R_p, which, for a given laser pulse, defines the constant *C*, which in turn defines the planetary surface area where the worst-case SNR is greater than 1. Clearly, relative to Earth, the SNR for a given lidar decreases for the inner planets, Mercury and Venus, and increases for the outer planets according to the equation

$$SNR_p = SNR_E \frac{R_P^2}{R_E^2} \quad (17)$$

The second and third parameters are the planetary mass and radius, which affect satellite altitude and velocity, and therefore the degree of overlap between successive laser pulses on the planetary surface. Table 2 lists the aforementioned parameters for the major planets in our solar system.

Table 2. Relevant parameters for the major planets in our solar system. The first row shows the distance of the planet from the Sun, which impacts the solar irradiance. The second row shows the increase (Mercury and Venus) or decrease (the outer planets) in the solar irradiance relative to Earth entering the planetary atmosphere. The third and fourth rows provide the mass and radius of the planets required to compute satellite orbital velocities. The values in the final row must be divided by the factor $\sqrt{1+z/r_P}$ in order to obtain the satellite orbital velocity at altitude z as presented in Equation (15).

	Mercury	**Venus**	**Earth**	**Mars**	**Jupiter**	**Saturn**	**Uranus**	**Neptune**
Solar Distance *Rp* (AU)	0.39	0.72	1	1.52	5.2	9.54	19.2	30.6
$(R_E/R_P)^2$	6.58	1.93	1.00	0.433	0.037	0.110	0.0027	0.00107
Mass M_P (kg)	3.28×10^{23}	4.87×10^{24}	5.97×10^{24}	6.39×10^{23}	1.89×10^{27}	5.68×10^{26}	8.68×10^{25}	1.02×10^{26}
Planetary Radius r_p (km)	2440	6052	6371	3390	66,911	58,232	25,362	24,622
Maximum Velocity (km/s)	3.01	7.33	7.91	3.55	42.6	25.5	15.1	16.7

10. Summary

In this paper, we have demonstrated that transmitting a single Gaussian lidar beam from an orbiting spacecraft and projecting the received image onto a highly pixelated detector can increase the number of measurements per pulse by one to two orders of magnitude with equal spatial resolution in both the along-track and cross-track directions whereas prior approaches like splitting the beam into multiple beamlets significantly degrades the cross-track spatial resolution and can also negatively impact penetration of tree canopies and water bodies by reducing the Signal to Noise Ratio (SNR). Furthermore, extending the observed surface area per pulse and number of pixels by a factor of 2 to record returns beyond the rare (i.e., twice per year) worst case minimum SNR situations can double the number of measurements per pulse when the solar background is reduced, for example at: (1) latitudes with higher values of secφ, (2) under night or twilight conditions (i.e., 50% or more of the satellite Earth orbit depending on angle θ), and (3) for values of θ approaching 90 or 180 degrees as the Earth orbits the Sun. Furthermore, even at or near worst-case solar background conditions, spatial correlation of photons outside the SNR = 1 boundaries with easily recognizable returns within multiple adjacent SNR = 1 boundaries becomes more likely.

Specific numerical results were then obtained assuming the ATLAS laser on NASA's ICESat-2 satellite as the source. Because of the high peak power of the ATLAS laser (E/τ_p = 333 kW) and its beneficial effect on the value of the constant C and the lidar SNR, a large surface area per pulse (up to 95 m $\times$ 95 m) can be monitored with a small (<2 mm) transmitted beam diameter from the ICESat-2 orbital altitude of 500 km. Since the combination of a large surface beam diameter with a high laser pulse rate (10 kHz) would result in an extremely large number of scientifically useless beam overlaps in the along-track direction, one can instead choose to greatly extend the cross-track coverage by scanning the transmitted beam. Furthermore, instead of greatly expanding the size of the detector array in the cross-track direction to accommodate the lengthy scans, one can choose to use a coordinated pair of scanners to compensate for point-ahead effects between the transmitted and received beams such that the received beam is always incident on a fixed 14 $\times$ 14 pixel detector array. The latter array provides between 100 and 196 measurements per pulse, depending on the solar background. Scanning large surface areas from space can be accomplished by either (1) scanning the small diameter transmit beam over a large circle using a pair of wedge scanners or (2) using a pair of Acousto-Optic Deflectors (AOD) scanning in a unidirectional linear nearly cross-track direction. In either case, the maximum physical length of the circle diameter or the cross-track scan for the ATLAS lidar would be equal to n_c d_{exp} = 124 $\times$ 95 m = 11.8 km, with equal along-track and cross-track spatial resolutions per pixel of $d_{exp}./14$ = 6.8 m.

A single dual-wedge scanner, operating on both the transmit and receive beams, has been used successfully in a number of commercial multibeam airborne lidars [5]. At aircraft altitudes, however, the receive telescope diameter can be fairly small and one of the wedges is annular so that

the transmit beam passes through the annulus and encounters only one wedge, while the receive beam is redirected by both wedges in order to achieve the necessary point-ahead compensation. The dual wedge scanner also directs the received photons to the common pixelated array, but the annulus introduces some loss to the received signal.

In 2002, the present author proposed a conceptual design, reproduced in Figure 8, that extended this annular dual wedge scanner technique to a spaceborne lidar by utilizing a larger Cassegrain receive telescope equipped with an annular secondary mirror and a transmitter collimating lens [3]. However, losses in signal strength caused by the annulus in the secondary mirror would be expected to affect the received lidar and solar photons equally resulting in no degradation in SNR. On the other hand, the annulus in the TR mirror could negatively impact signal strengths seen by pixels near the center of the array. Therefore, it is likely advantageous to use a pair of co-aligned transmit and receive telescopes [7], each equipped with its own internal single wedge scanner for conical scans or with separate AODs for linear scans. As before, the length and timing of the scan angle commands for each AOD must be adjusted to compensate for both the roundtrip pulse TOF and the individual telescope magnifications. As discussed in Section 7 of the current paper, extending the circular scan to spacecraft altitudes, while likely easier to implement, would require more extensive data post-processing to generate the desired, large area 3D surface maps than the linear-scan approach using two AOD devices.

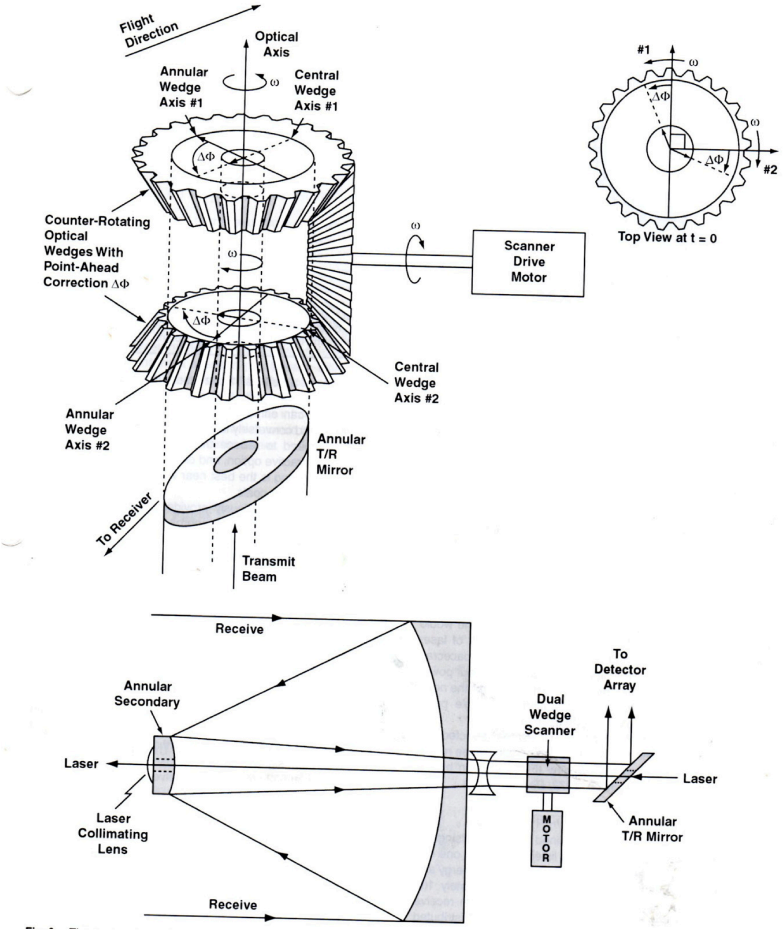

Figure 8. The dual wedge optical scanner with point-ahead compensation consists of two counter-rotating optical wedges. A central core in each wedge is advanced in rotational phase relative to the outer wedge in order to point the transmitter to the spot where the receiver will be looking one round trip transit time later. The figure includes an example of how a smaller scanner can be placed internal to the instrument behind a conventional Cassegrain receive telescope. The wedge angles in the internal scanner must be enlarged, relative to an external scanner in front of the telescope, to compensate for the 1/M reduction in the offset angle from nadir where M is the telescope magnification (Ref. [3]).

In closing, Table 2 provides key parameters to support potential future use of the proposed single-beam technique on lidar missions to other planets in our solar system or, perhaps more importantly, their moons. A recent review article provides a summary of past spaceborne lidars [15]. Future interplanetary missions may benefit from the use of compact, high-peak-power, passively Q-switched microlasers, which have recently been shown to achieve peak powers and multi-kHz pulse rates comparable to the much larger ATLAS laser [16–18]. Although photomultipliers have already been used successfully in a wide variety of space missions, a recent review article describes the wavelength suitability and current space-qualification status of other detector array types, such as SPADs and GMAPDs [19]. Potential methods for continuously gathering and transmitting many Megabits of lidar data over interplanetary distances and over long periods of time, via quasi-synchronous parallel orbits between Earth and the planet being mapped, have been discussed in a previous paper by the author [7].

Funding: This research received no external funding.

Data Availability Statement: Not applicable.

Conflicts of Interest: The author declares no conflicts of interest.

References

1. Degnan, J.J.; McGarry, J.F.; Dabney, P.; Zagwodzki, T.W. Design and Performance of an Airborne Multi-kilohertz Photon-Counting Microlaser; Altimeter. *Int. Arch. Photogramm. Remote Sens. Spat. Inf. Sci.* **2001**, *34*, 9.
2. Degnan, J.J. Photon-counting multikilohertz microlaser altimeters for airborne and spaceborne topographic measurements. *J. Geodyn.* **2002**, *34*, 503. [CrossRef]
3. Degnan, J.J. A conceptual design for a spaceborne 3D imaging lidar. *e&i Elektrotechnik Informationstechnik* **2002**, *119*, 99. [CrossRef]
4. Marino, R.M.; Davis, R.M., Jr. Jigsaw: A Foliage- Penetrating 3D Imaging Laser Radar System. *Linc. Lab. J.* **2005**, *15*, 23.
5. Degnan, J.J. Scanning, multibeam, single photon lidars for rapid, large scale, high resolution topographic and bathymetric mapping. *Remote Sens.* **2016**, *8*, 958. [CrossRef]
6. Neumann, T.A.; Martino, A.J.; Markus, T.; Bae, S.; Bock, M.R.; Brenner, A.C.; Brunt, K.M.; Cavanaugh, J.; Fernandes, S.T.; Hancock, D.W.; et al. The Ice, Cloud, and Land Elevation Satellite-2 mission: A global geolocated photon product derived from the Advanced Topographic Laser Altimeter System. *Remote Sens. Environ.* **2019**, *233*, 111325.
7. Degnan, J.J. Extending the ICESat-2 ATLAS Lidar Capabilities to Other Planets Within Our Solar System. *Photonics* **2025**, *12*, 1048. [CrossRef]
8. Available online: https://en.wikipedia.org/wiki/Solar_irradiance (accessed on 22 June 2026).
9. Kogelnik, H. On the Propagation of Gaussian Beams of Light Through Lenslike Media Including those with a Loss or Gain Variation. *Appl. Opt.* **1965**, *4*, 1562. [CrossRef]
10. Romer, G.R.B.E.; Bechtold, P. Electro-optic and acousto-optic laser beam scanners. *Phys. Procedia* **2014**, *29*, 29–39.
11. Duma, V.F.; Duma, M.A. Optomechanical Analysis and Design of Polygon Mirror-Based Laser Scanners. *Appl. Sci.* **2022**, *12*, 5592. [CrossRef]
12. Roy, P. Acousto-Optic Deflector- Principles, Working, and Applications. *Int. J. Adv. Netw. Appl.* **2023**, *15*, 6126.
13. Available online: https://www.cq-smart.com/acousto-optic-deflectors-principles-applications-and-resolution (accessed on 22 June 2026).
14. Available online: https://www.l3harris.com/sites/default/files/2024-08/l3harris-model-h-424-acousto-optic-deflector-spec-sheet-sas.pdf (accessed on 22 June 2026).
15. Bolcek, J.; Barakat, M.A.; Veverka, J.; Sloboda, S.; Marsalek, R.; Gotthans, T. Spaceborne Lidar Systems: Evolution, Capabilities and Challenges. *Sensors* **2025**, *25*, 3696. [CrossRef] [PubMed]
16. Degnan, J.J. Optimization of Passively Q-switched Lasers. *IEEE J. Quantum Electron.* **1995**, *31*, 890. [CrossRef]
17. Chen, J.; Wang, Y.; Chen, X.; Cheng, G.; Wu, Y.; Zhao, X.; Gao, H.; Shang, L.; Zhang, T.; Liu, P.; et al. Dual single-emitter diode pumped Q-switched Nd:YAG MOPA laser for wind lidar. *Opt. Express* **2026**, *12*, 21174.
18. Sub-ns Passively Q-Switched Microchip Solid State Lasers. Available online: https://www.alphalas.com/ (accessed on 22 June 2026).
19. Sun, X. Review of Photodetectors for Space Lidars. *Sensors* **2024**, *24*, 6620. [CrossRef] [PubMed]

Disclaimer/Publisher's Note: The statements, opinions and data contained in all publications are solely those of the individual author(s) and contributor(s) and not of MDPI and/or the editor(s). MDPI and/or the editor(s) disclaim responsibility for any injury to people or property resulting from any ideas, methods, instructions or products referred to in the content.